Low-Switching-Frequency Operation of a Modular Multilevel DSCC Converter With Phase-Shifted Rotating-Carrier PWM

Firman Sasongko, *Student Member, IEEE*, and Hirofumi Akagi, *Fellow, IEEE*

***Abstract*—This paper provides a theoretical discussion on a new phase-shifted rotating-carrier (PSRC) pulsewidth modulation (PWM) method for a modular multilevel double-star chopper-cell (DSCC) converter. The new method enables the DSCC converter to operate at a low switching frequency in a range of 50 to 100 Hz where the ac grid or line frequency is 50 Hz. The phase shift of each carrier signal is rotated to enable capacitor–voltage balancing in such a low-carrier-frequency range while maintaining the same voltage in each arm as that of the original phase-shifted-carrier PWM. Theoretical analysis of harmonic-voltage spectrum at the arm side of a chopper cell is conducted on the basis of double-variable Fourier series. Then, the analytical results are compared to numerical ones. A three-phase grid-connected DSCC converter rated at 66 kV, 50 Hz, and 100 MW with 64 chopper cells per leg is used in circuit simulation to confirm the validity of the proposed PSRC-PWM method. The simulation results show that the PSRC-PWM can maintain stable operation of the DSCC converter even if the carrier frequency goes lower than 100 Hz. Several performance criteria conclude that the optimal carrier frequency is 75 Hz.**

***Index Terms*—Grid connections, low carrier frequencies, modular multilevel cascade converters (MMCCs), pulsewidth modulation (PWM).**

I. Introduction

In HIGH-POWER and high-voltage applications, any converter should be designed to have high efficiency. Therefore, the switching frequency of the converter should be set as low as possible to reduce switching power loss [1]–[3]. One of the advantages of multilevel converters over two-level or three-level converters is that the equivalent switching frequency of the ac-terminal voltage can be much higher than the actual switching frequency of the submodules or cells used in the multilevel converters. Thus, no harmonic filter is installed at the grid side because of much better voltage quality [4]–[6].

The modular multilevel cascade converter (MMCC) family has gained more attention recently for high-power applications [2]–[10]. Because of modularity and redundancy of the chopper or bridge cells used in the MMCC family, the number of series-connected cells can be adjusted easily to meet the desired voltage rating of the converter. Among the several family members, the modular multilevel double-star chopper-cell (DSCC) converter is suitable for grid connections and motor drives [10]. This converter is also referred to just as a modular multilevel converter (MMC) [7]–[9]. The DSCC converter can use either carrier-based or noncarrier-based (programmed) pulsewidth modulation (PWM) to generate three-phase ac-terminal voltages [4]–[6], [11]–[25]. Noncarrier-based PWM methods [20]–[25] may allow low-switching-frequency operation at the expense of increasing complexity of the algorithms as the number of chopper cells increases. On the other hand, carrier-based PWM methods [13]–[20] are usually used with a higher switching frequency that leads to a higher switching power loss.

Several recent publications have addressed various noncarrier-based PWM methods for the DSCC converter for grid connections, with focus on lower switching frequencies [26]–[30]. The switching frequencies can be as low as the ac grid frequency by using the so-called "nearest voltage-level control" modulation method [26]–[28], or a new modulation method proposed in [29]. Another modulation method based on "tolerance band" can also produce a low switching frequency that is close to the ac grid frequency [30]. However, the actual switching frequency is not constant because it depends on the operating conditions.

A few attempts have discussed carrier-based PWM to operate at low switching frequencies [31]–[33]. However, no literature has discussed the use of carrier-based PWM that is comparable to the aforementioned noncarrier-based PWM in terms of actual switching frequency. It is even stated that carrier-based PWM cannot be used with carrier frequencies lower than 100 Hz, where the ac grid frequency is 50 Hz [30].

This paper proposes a new carrier-based PWM method for a DSCC converter, which is referred to as phase-shifted rotating-carrier (PSRC) PWM throughout this paper. It results from general phase-shifted-carrier (PSC) PWM. The phase shift of each carrier is rotated in such a way that the voltage across each arm of the converter remains the same as that of the PSC-PWM. This paper also conducts theoretical analysis of the voltage waveform at the arm side of a chopper cell that applies the PSRC-PWM based on double-variable Fourier series. The PSRC-PWM enables capacitor-voltage balancing, and

Manuscript received June 10, 2016; revised August 6, 2016; accepted September 5, 2016. Date of publication September 13, 2016; date of current version February 27, 2017. Recommended for publication by Associate Editor M. A. Perez.

F. Sasongko is with the Department of Electrical and Electronics, Tokyo Institute of Technology, Tokyo 152-8550, Japan (e-mail: firman.s@akg.ee.titech.ac.jp).

H. Akagi is with the Department of Electrical and Computer Engineering, Tokyo Institute of Technology, Tokyo 152-8552, Japan (e-mail: akagi@ee.titech.ac.jp).

Color versions of one or more of the figures in this paper are available online at http://ieeexplore.ieee.org.

Digital Object Identifier 10.1109/TPEL.2016.2608912

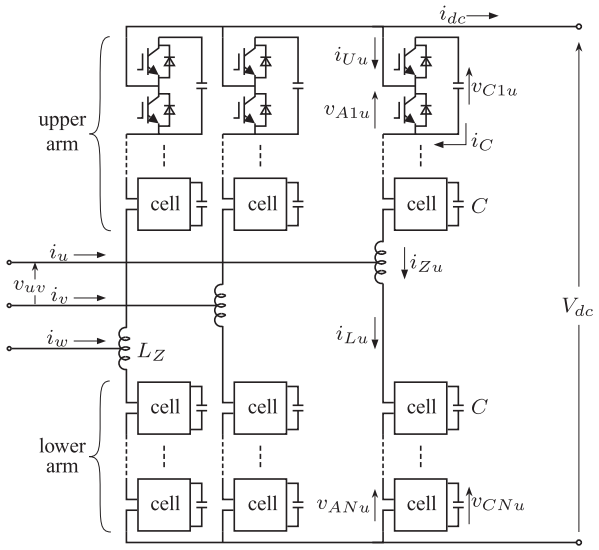

Fig. 1. Circuit configuration of a three-phase DSCC converter with N chopper cells per leg.

equalizes all the chopper cells in power distribution at low-carrier-frequency operation. Circuit simulation using the software package of PSCAD/EMTDC confirms the validity of the PSRC-PWM under a three-phase grid-connected DSCC converter rated at 66 kV, 50 Hz, and 100 MW with 64 chopper cells per leg. The DSCC converter based on the PSRC-PWM results in providing good performance even if the carrier frequency is set in a range of 50–100 Hz. Several carrier frequencies in the range are compared based on several criteria. This paper concludes that the optimal carrier frequency is 75 Hz in a range of 50–100 Hz.

II. A PSC-PWM-Based DSCC Converter

A. Circuit Configuration

Fig. 1 shows the circuit configuration of a three-phase DSCC converter consisting of N series-connected chopper cells and a center-tapped inductor L_Z per phase leg. The ac-terminal voltage waveform contains $N+1$ and $2N+1$ levels in maximum at the line-to-neutral and line-to-line voltages, respectively. For grid connections, an ac-link inductor in each phase should be connected between the ac grid terminal and the center terminal of the center-tapped inductor L_Z to support the voltage difference between the two terminals. In the following discussion, only the u-phase leg is mentioned, because the other two phases can be treated similarly.

There are two independent currents in each phase leg, i.e., the circulating current i_{Zu} and the line current i_u. Therefore, the upper and lower arm currents that act as dependent currents can be expressed as follows [16]:

$$i_{\mathrm{Uu}} = -\frac{i_u}{2} + i_{\mathrm{Zu}}, \tag{1}$$

$$i_{\mathrm{Lu}} = \frac{i_u}{2} + i_{\mathrm{Zu}}. \tag{2}$$

Equations (1) and (2) show that the line-current component in the upper and lower arms are out of phase by 180° each other. Therefore, the inductor presents no inductance to the line current i_u, whereas it renders the inductance L_Z to the circulating current i_{Zu} that is flowing through all the chopper cells in the u-phase leg.

The PSC-PWM method assigns a triangular carrier signal for each chopper cell in the DSCC converter for grid connections. Let f_{ac} be the frequency of the reference signal for a chopper cell, which is equal to the ac grid frequency, M be the modulation index, $F_{\mathrm{tri}}(t)$ be a triangular function that has unity amplitude, and f_{cr} be the frequency of the carrier signal. The reference signal v_{ref} and the carrier signal v_{cr} can be described as follows:

$$v_{\mathrm{ref}} = \frac{1}{2} + \frac{M}{2}\cos(\omega_{\mathrm{ac}}t + \theta_{\mathrm{ac}}), \tag{3}$$

$$v_{\mathrm{cr}} = F_{\mathrm{tri}}(\omega_{\mathrm{cr}}t + \theta_{\mathrm{cr}}) \tag{4}$$

where θ_{ac} and θ_{cr} represent phase shifts of the reference and carrier signals, respectively, to an arbitrary point in time. The carrier signals in each arm of the DSCC are phase-shifted each other by $4\pi/N$. For instance, if (4) is assigned to a chopper cell in an arm of the DSCC, the two adjacent chopper cells in series have carrier phase shifts of $\theta_{\mathrm{cr}} + 4\pi/N$ and $\theta_{\mathrm{cr}} - 4\pi/N$. The carrier phase shift between the upper and lower arms in each phase leg is $2\pi/N$ to achieve harmonic-voltage cancellation.

A major advantage of the PSC-PWM combined with a closed-loop control is that the actual switching frequency of each chopper cell is equal to the carrier frequency regardless of operating conditions, circuit parameters, or control gains [16]. Note that the equivalent switching frequency for each leg is equal to $N \times f_{\mathrm{cr}}$. Moreover, the circuit behavior can be easily determined and analyzed because the circuit configuration can be modeled as a *linear* and *continuous* system [19], [32], [33].

The PSC-PWM-based DSCC converter utilizes a three-layer hierarchical control to balance the capacitor voltages [17]. The "individual balancing control" in the bottom layer regulates each capacitor voltage to the arithmetic-average voltage of $N/2$ capacitors per arm. A digital low-pass filter, including a moving-average filter, is necessary for the individual balancing control in order to extract the dc component from each capacitor voltage that contains ac components. The interaction of the arm-side voltage of a chopper cell and its arm current produces a dc component in the capacitor current, thus bringing dc-component deviation to the capacitor voltage. The individual balancing control has the ability to cancel out a small dc current, thus making the DSCC converter stable. However, the gain of the individual balancing control cannot be set to be too high to prevent overmodulation from each chopper cell.

B. Constraints on PSC-PWM at Low Carrier Frequencies

For high-power applications, it is desirable to utilize a carrier frequency as low as possible to minimize the switching power loss. It is quite feasible to operate the DSCC converter with a low-carrier-frequency ratio with respect to the ac grid frequency (CFR $= f_{\mathrm{cr}}/f_{\mathrm{ac}}$) because the equivalent carrier frequency of the ac-terminal voltage is still much higher than the

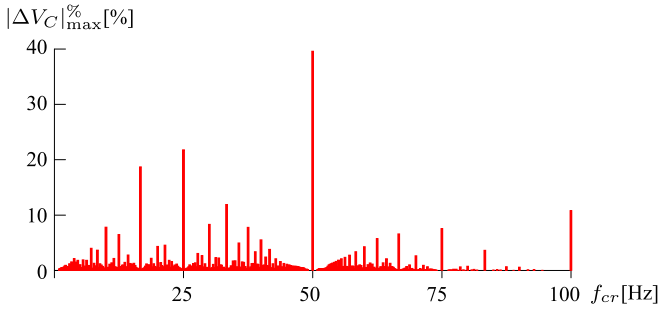

Fig. 2. Normalized maximum dc voltage deviation against the carrier frequency $f_{\rm cr}$.

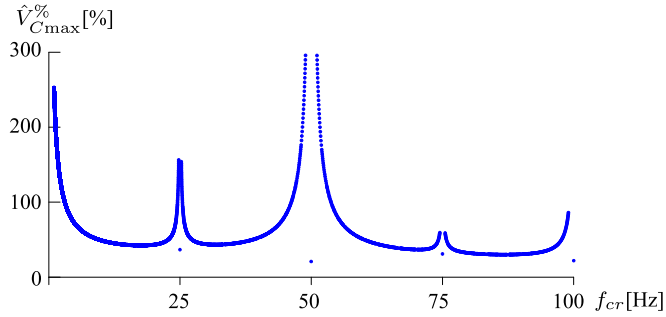

Fig. 3. Normalized maximum ac voltage fluctuation against the carrier frequency $f_{\rm cr}$.

TABLE I
PARAMETERS USED IN THE ANALYSIS

AC grid frequency	$f_{\rm ac}$	50 Hz
Unit capacitance constant	H_C [34]	40.8 ms
Per-unit ac-link inductance	$L_{\rm ac}^{\rm pu}$	0.1 pu
DC voltage/ac voltage	$V_{\rm dc}/V_{\rm ac}$	2
Active power/rated power	p/P	1
Reactive power/rated power	q/P	0

carrier frequency. However, there are several issues to be considered when a low CFR is utilized, especially when the carrier frequency is lower than double the ac grid frequency ($f_{\rm cr} < 2f_{\rm ac}$). In particular, the arm-side voltages of the chopper cells may become heavily distorted, and the capacitor voltages may deviate steadily, which causes unstable operation of the DSCC converter.

As the CFR gets lower, the arm-side voltage of each chopper cell includes larger sideband harmonic components around the carrier frequency. If one of the sideband harmonic frequencies coincide with the ac grid frequency or the zero (dc) frequency, serious voltage distortion occurs in the arm-side voltage of each chopper cell. The amplitudes of the sideband harmonic-frequency components depend on the carrier phase shift $\theta_{\rm cr}$ and the modulation index M. These dependencies create a problem in the PSC-PWM-based DSCC converter that uses many carrier signals with different carrier phase shifts. The fundamental-frequency (grid-frequency) and dc components included in the arm-side voltages of the chopper cells may differ, thus resulting in power imbalances among the chopper cells.

Fig. 2 shows analytical values of the normalized maximum dc-voltage deviation $|\Delta V_C|^{\%}_{\max}$ occurring in the capacitor voltage v_C of a chopper cell when the carrier frequency $f_{\rm cr}$ ranges from 0 to 100 Hz with the ac grid frequency $f_{\rm ac}$ of 50 Hz. The result in Fig. 2 is obtained by using the analytical approach described in [33], along with the parameters listed in Table I. The analytical result shows that significant dc voltage deviations occur at carrier frequencies that are multiples of one-half and one-third of the ac grid frequency. Note that their amplitudes also depend on both the carrier phase shift $\theta_{\rm cr}$ and the modulation index M. The individual balancing control has the function of eliminating the dc voltage deviations. However, it cannot maintain the mean dc voltage of the capacitor to the nominal value when the dc voltage deviations become too large.

Fig. 3 shows the analytical values of the normalized maximum ac-component fluctuation $\hat{V}^{\%}_{C\max}$ in the capacitor voltage of a chopper cell, using the same circuit parameters as those in Fig. 2. It is interesting to note that although the analytical values are significantly large at the carrier frequencies close to multiples of one-half of the ac grid frequency, they are the lowest at the exact carrier frequencies of one-half multiples of the ac grid frequency. Nevertheless, carrier frequencies that are equal to or very close to the ac grid frequency of 50 Hz should be avoided because large dc-component deviation ΔV_C and/or serious ac-component fluctuation $\hat{V}_{C\max}$ may occur.

Using a low CFR may also result in causing the so-called "multi-switchings" in which more than one pulse are generated in a single carrier period. A frequency-ratio boundary CFR_B is defined as a carrier-ratio limit in which no occurrence of the multiswitchings can be guaranteed. For a naturally sampled PWM method, the frequency-ratio limit can be expressed as follows:

$$\mathrm{CFR}_B = \frac{f_{\rm crB}}{f_{\rm ac}} = M\frac{\pi}{2}. \tag{5}$$

This multiswitchings issue may not be accepted in many applications because it makes the actual switching frequency higher than the carrier frequency.

III. PHASE-SHIFTED ROTATING-CARRIER PWM

A. Basic Principles

The PSC-PWM method assigns one triangular carrier signal with an appropriate fixed phase shift to one chopper cell. On the other hand, the PSRC-PWM method assigns it with a variable phase shift that is rotating within a carrier-signal period of 2π.

Fig. 4 illustrates carrier-phase-shift rotation for chopper cells in an arm. The carrier phase shift $\theta_{\rm cr}$ of a chopper cell is basically changed to a phase shift used by the carrier of the adjacent chopper cell in the previous carrier period. The rotation angle δ, shown in Fig. 4, depends on the number of chopper cells per leg, N, as follows:

$$\delta = \frac{4\pi}{N}. \tag{6}$$

The angular velocity ω_r expresses the rotation speed at which the phase shift of the carrier in a chopper cell is changed. It should be noted that the rotation of the phase shift occurs at

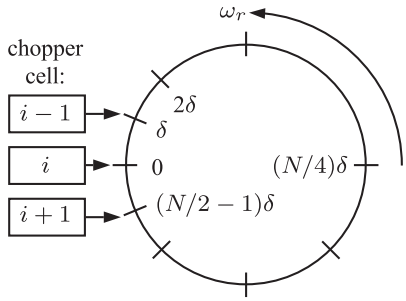

Fig. 4. Carrier phase-shift rotation for chopper cells in an arm.

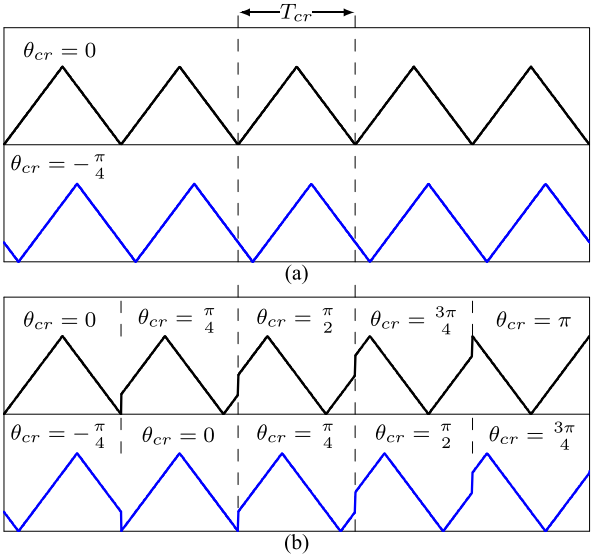

Fig. 5. Two triangular carrier waveforms that are phase-shifted by $\pi/4$. (a) No phase-shift rotation. (b) Rotating by $\pi/4$.

discrete steps. The rotation speed ω_r can be related to the carrier frequency $f_{\rm cr}$ as follows:

$$\omega_r = \frac{4\pi f_{\rm cr}}{N}. \tag{7}$$

Fig. 5(a) depicts two triangular carrier waveforms that are phase-shifted by $\delta = \pi/4$ in the PSC-PWM method, whereas Fig. 5(b) depicts those with a rotation angle of $\delta = \pi/4$ in the PSRC-PWM method. All carrier signals in an arm of the DSCC converter undergo all the phase shifts used in the arm. The carrier-phase-shift rotation occurs at the same instant for all chopper cells every carrier period $T_{\rm cr}$. Therefore, each arm voltage in the PSRC-PWM method is the same as that in the PSC-PWM method under the assumption of no dead time.

B. Analytical Approach

The PWM process can be analyzed and explained by using a three-dimensional geometrical model in conjunction with Fourier series in two variables [35]–[37]. The x- and y-axes represent the two frequency variables that are periodic in their respective axis. The z-axis represents the height of the model and can be expressed as a wall function of the two variables, $F(x, y)$. A PWM signal waveform with a frequency ratio of

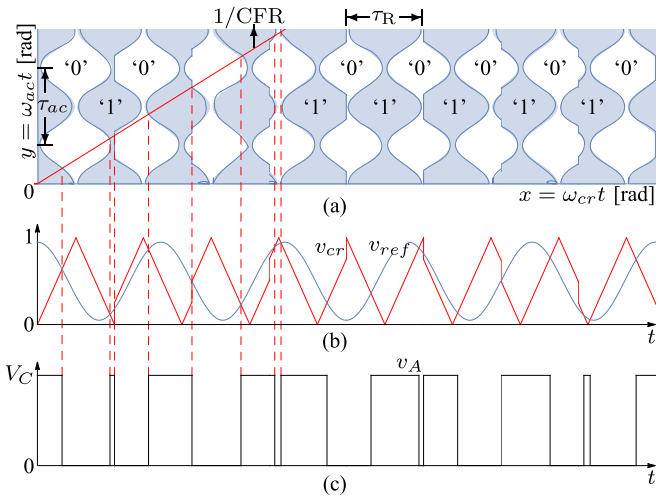

Fig. 6. Geometrical representation of a full-rotation period in a two-level naturally sampled rotating-carrier PWM for CFR $= 8/5$, $\delta = \pi/4$, and $M = 0.9$. (a) The xy-plane. (b) Reference and carrier signals. (c) The resulting PWM signal at the arm-side voltage of a chopper cell, v_A.

$f_{\rm ac}/f_{\rm cr}$ $(= 1/\text{CFR})$ can be synthesized by projecting the intersections of the wall function with the frequency-ratio plane $f_{\rm ac}/f_{\rm cr}$ to the $x0z$-plane. To analyze a rotating-carrier PWM signal waveform, the frequency-ratio plane should be adjusted to match the rotating-carrier waveform that has a noncontinuous function (see the Appendix).

The switching frequency of the rotating-carrier PWM method is unequal to the carrier frequency $f_{\rm cr}$ because of the rotation angle δ. Based on the rotating-carrier angular cycle τ_R defined by (19) in the Appendix, the equivalent switching frequency $f_{\rm sw}$ can be expressed as

$$f_{\rm sw} = f_{\rm cr}\left(1 + \frac{\delta}{2\pi}\right). \tag{8}$$

Equation (8) can also be related to the number of chopper cells per leg, N, as follows:

$$f_{\rm sw} = f_{\rm cr}\left(1 + \frac{2}{N}\right). \tag{9}$$

Equation (9) shows that the equivalent switching frequency $f_{\rm sw}$ is incremented by a factor of $2/N$ from the carrier frequency $f_{\rm cr}$. The equivalent switching frequency $f_{\rm sw}$ gets closer to the carrier frequency $f_{\rm cr}$ as the number of chopper cells per leg increases.

The rotating-carrier PWM method produces a periodic carrier signal in several carrier cycles instead of one carrier cycle. If the rotation angle δ is set in accordance with (6), the modulation method requires $N/2$ rotation steps to complete a full rotation of 2π that produces a periodic carrier signal. Equation (6) shows that as the number of chopper cells per leg of the DSCC converter gets higher, the carrier signals experience a very small phase shift for each carrier period, and the waveforms look more similar to those of the nonrotating triangular carriers. However, the time period to complete a full rotation of 2π gets longer.

Fig. 6(a) shows a geometrical representation of the rotating-carrier wall function $F_R(x, y)$ for a full-rotation period when

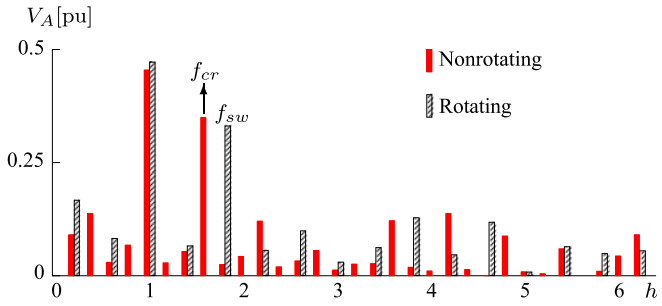

Fig. 7. Comparison in harmonic-voltage spectrum at the arm side of a chopper cell between nonrotating-carrier and rotating-carrier PWM methods at $\mathrm{CFR} = 8/5$, $\delta = \pi/4$, and $M = 0.9$ for several harmonic orders h.

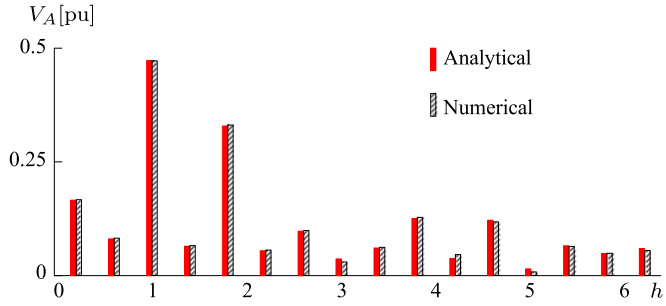

Fig. 8. Comparison between analytical and numerical results in harmonic-voltage spectrum at the arm side of a chopper cell when the rotating-carrier PWM method is used at $\mathrm{CFR} = 8/5$, $\delta = \pi/4$, and $M = 0.9$ for several harmonic orders h.

the rotating-carrier PWM has a rotation angle of $\delta = \pi/4$. In the two-dimensional model of double-edge naturally sampled PWM, Fig. 6(a) consists of a wall function for nine carrier angular cycles ($9\tau_{\mathrm{cr}} = 18\pi$). However, because the rotation of δ removes the stripped areas (see the Appendix), the new wall functions are not identical anymore for each angular cycle. Therefore, Fig. 6(a) actually consists of eight different wall functions each of which has an angular cycle of τ_R, as defined by (19) in the Appendix. Moreover, the frequency-ratio slope becomes ordinary, and makes the mathematical integration process easier. Note that the rotating-carrier PWM method does not alter the frequency-ratio boundary CFR_B defined in (5).

Fig. 6(b) shows the reference waveform v_{ref} and the rotating-carrier signal waveform v_{cr} as the projection of the rotating-carrier wall function in Fig. 6(a) into the time domain. Fig. 6(c) shows the resulting PWM signal waveforms from Fig. 6(a) and (b) with a capacitor voltage of V_C.

Fig. 7 shows a comparison in harmonic-voltage spectrum at the arm side of a chopper cell between nonrotating-carrier and rotating-carrier PWM methods under the same parameters as those in Fig. 6. Note that the magnitudes of the harmonic components in Fig. 7 are normalized with respect to the capacitor voltage V_C. The harmonic-voltage spectrum of the rotating-carrier PWM is modified due to the phase-shift rotation in the carrier (see the Appendix).

The nonrotating-carrier PWM results in a fundamental-frequency component, carrier-harmonic components and their sideband-harmonic components. The carrier-harmonic components appear only at odd numbers of the carrier index variable m. For odd numbers of m, the sideband-harmonic components appear at even numbers of the reference index variable n. For even number of m, the sideband-harmonic components appear at odd numbers of n.

The rotating-carrier PWM also produces similar frequency components. However, the carrier index variable of the rotating-carrier PWM is no longer equal to m. Instead, it becomes $2m/N$ because of phase-shift rotation. Because of the $\mathrm{CFR} = 8/5$, the harmonic-voltage spectrum of the nonrotating-carrier PWM consists of sideband-harmonic components of which frequencies are integer multiples of 10 Hz. On the other hand, the rotating-carrier PWM consists of sideband-harmonic components of which frequencies coincide with the carrier-harmonic frequencies, that is, the odd multiples of 10 Hz. The total harmonic distortion in voltage (THD_v) in the nonrotating-carrier PWM is 115.6%, whereas that in the rotating-carrier PWM is 108.1%. The equivalent CFR of the rotating-carrier PWM becomes 9/5 for $\delta = \pi/4$.

Fig. 8 shows a comparison in harmonic-voltage spectrum of the rotating-carrier PWM between analytical and numerical methods. The analytical method uses (20)–(28), that are derived in the Appendix, whereas the numerical method uses fast Fourier transform of a rotating-carrier PWM signal that is generated by using a spreadsheet program with a time step of 1 μs. Fig. 8 shows that the two results are almost identical, confirming the harmonic-voltage equation of the rotating-carrier PWM method (see the Appendix).

C. DC-Component Reduction in Capacitor Voltage

As shown in Fig. 2, the dc-component deviation in the capacitor voltage of a chopper cell can be evaluated by using the capacitor current i_C that is given as a product of the arm current and the PWM switching function [33]. Using (2), along with (20) in the Appendix, yields the capacitor current i_C of a chopper cell assigned to a rotating-carrier signal in the lower arm as follows:

$$\begin{aligned} i_C = {} & \hat{I}_{\mathrm{C1}} \cos(\omega_{\mathrm{ac}} t + \phi_{\mathrm{ac}}) + \frac{\hat{I}_u M}{8} \cos(2\omega_{\mathrm{ac}} t + \theta_{\mathrm{ac}} + \theta_i) \\ & + \sum_{\mathrm{m}=1}^{\infty} |C_{\mathrm{m}0}| \Big(I_{\mathrm{Zu}} \cos\left(m'\omega_{\mathrm{cr}} t + \theta_{\mathrm{m}0}\right) \\ & + \frac{\hat{I}_u}{4} \cos\left(m'\omega_{\mathrm{cr}} t \pm \omega_{\mathrm{ac}} t + m'\theta_{\mathrm{m}0} \pm \theta_i\right) \Big) \\ & + \sum_{\mathrm{m}=1}^{\infty} \sum_{\substack{n=-\infty \\ n\neq 0}}^{\infty} |C_{\mathrm{mn}}| \Big(I_{\mathrm{Zu}} \cos\left(m'\omega_{\mathrm{cr}} t + n\omega_{\mathrm{ac}} t + \theta_{\mathrm{mn}}\right) \\ & + \frac{\hat{I}_u}{4} \cos\left(m'\omega_{\mathrm{cr}} t + (n \pm 1)\omega_{\mathrm{ac}} t + \theta_{\mathrm{mn}} \pm \theta_i\right) \Big) \end{aligned} \tag{10}$$

where m and n are index variables for the carrier and reference signals, respectively, $C_{\mathrm{m}0}$, C_{mn}, $\theta_{\mathrm{m}0}$, and θ_{mn} are given by (21)–(24) in the Appendix, $\hat{I}_u$ and θ_i are the amplitude peak value and the phase of the u-phase line current i_u, I_{Zu} is the dc

component present in the circulating current i_{Zu}, and $\hat{I}_{\mathrm{C1}}$ and ϕ_{ac} are given by

$$\hat{I}_{\mathrm{C1}} = \frac{1}{2}\sqrt{M^2 I_{\mathrm{Zu}}^2 + \frac{\hat{I}_u^2}{4} + M I_{\mathrm{Zu}} \hat{I}_u \cos(\theta_{\mathrm{ac}} - \theta_i)}, \quad (11)$$

$$\phi_{\mathrm{ac}} = \tan^{-1} \frac{2M I_{\mathrm{Zu}} \sin\theta_{\mathrm{ac}} + \hat{I}_u \sin\theta_i}{2M I_{\mathrm{Zu}} \cos\theta_{\mathrm{ac}} + \hat{I}_u \cos\theta_i}. \quad (12)$$

Equation (10) shows that the equivalent index variable for the carrier is modified to $m' = 2m/N$. This result means that the harmonic-current components included in i_C for the rotating-carrier PWM are different in center frequencies from those for the nonrotating-carrier PWM. An individual harmonic-current component in (10) may become a dc-current component when the interaction between carrier-harmonic and sideband-harmonic frequencies results in producing a zero (dc) frequency. The dc-component deviation in the capacitor voltage is caused by the total dc-current component contained in i_C. An individual dc-current component can be obtained from (10) by satisfying one of the following equations:

$$\frac{2m}{N}\omega_{\mathrm{cr}} - \omega_{\mathrm{ac}} = 0 \quad (13)$$

$$\frac{2m}{N}\omega_{\mathrm{cr}} - n\omega_{\mathrm{ac}} = 0 \quad (14)$$

$$\frac{2m}{N}\omega_{\mathrm{cr}} - (n \pm 1)\omega_{\mathrm{ac}} = 0. \quad (15)$$

Equations (13)–(15) express a specific condition in which any sideband harmonic frequency has a zero value, that is, produces a dc-current component. Note that the three equations show only the frequencies of the sideband-harmonic-frequency components without showing any amplitude information. Let the irreducible fraction of the ac grid and carrier frequencies be f'_{ac} and f'_{cr}, respectively, and a positive integer be g. The solutions to (13)–(15) are given as follows:

$$(m,n) = \begin{cases} \left(\frac{N}{2}\frac{f'_{\mathrm{ac}}}{f'_{\mathrm{cr}}}, 0\right) & \text{for } n = 0 \\ \left(g\frac{N}{2}f'_{\mathrm{ac}}, gf'_{\mathrm{cr}}\right) & \text{for } n \neq 0 \\ \left(g\frac{N}{2}f'_{\mathrm{ac}}, gf'_{\mathrm{cr}} \mp 1\right), & \text{for } n \neq 0. \end{cases} \quad (16)$$

Equation (16) shows that the solution regarding m is obtained by multiplying the integer g with the number of chopper cells per arm $N/2$ and the irreducible fraction of the ac grid frequency f'_{ac}. Thus, m becomes higher as N gets higher. Moreover, the amplitude of the individual dc-current component becomes much smaller and can be ignored because it is inversely proportional to m, as shown in (21) and (22) in the Appendix. This outcome explains why the PSRC-PWM method can suppress significantly the dc-component deviation occurring in the capacitor voltage of a chopper cell even if a low CFR is used.

D. Phase-Shift-Dependency Cancellation

Fig. 9 shows a comparison in the normalized fundamental-frequency component of the arm-side voltage of the chopper cell between the rotating-carrier and nonrotating-carrier PWM methods at $\mathrm{CFR} = 3/2$. It can be seen that the fundamental component in the nonrotating-carrier PWM fluctuates, depending on the carrier phase shift θ_{cr}. The fluctuation occurs because of the interferences with the sideband harmonic components that have the same harmonic frequency as the fundamental frequency. On the other hand, the rotating-carrier PWM produces a relatively constant amplitude of the fundamental component. Note that the rotating-carrier PWM uses a rotation angle $\delta = 11.25°$. The effect of dependency on the carrier phase shift can be minimized significantly as the rotation angle gets closer to zero because each carrier signal experiences all the possible phase shifts almost linearly within a carrier-signal period of 2π.

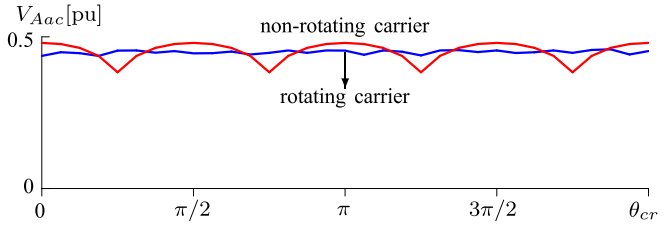

Fig. 9. Comparison in normalized fundamental-frequency component of the arm-side voltage of a chopper cell V_{Aac} between nonrotating-carrier and rotating-carrier PWM methods at $\mathrm{CFR} = 3/2$ and $M = 0.9$, using naturally sampled PWM.

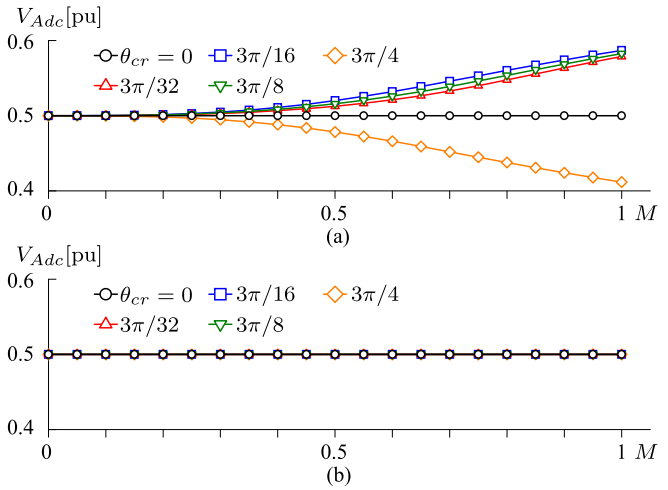

Fig. 10. Normalized dc-voltage component at the arm side of a chopper cell, V_{Adc}, at $\mathrm{CFR} = 3/2$. (a) Nonrotating carrier. (b) Rotating carrier.

Fig. 10 shows a comparison in the normalized dc-voltage component at the arm side of a chopper cell between rotating-carrier and nonrotating-carrier PWM methods. The DSCC converter has to guarantee that each chopper cell produces the same dc-voltage component at the arm side to balance the dc-voltage component across the phase legs and power distribution in the chopper cells. It is impossible to tolerate a significant change in the dc-voltage component caused by a slight change in the carrier phase shift θ_{cr} or the modulation index M. It is helpful to use a uniform PWM method to avoid dc-voltage component deviation. However, this benefit might make a compromise with the fundamental-voltage component at the arm side of

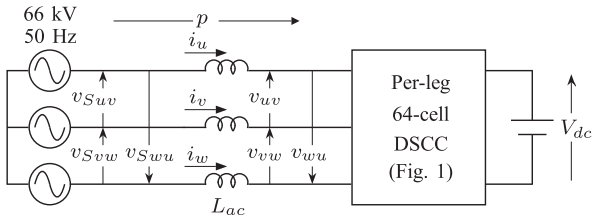

Fig. 11. Circuit diagram of a grid-connected DSCC converter consisting of 64 chopper cells per leg.

TABLE II
CIRCUIT PARAMETERS FOR SIMULATION

Rated power	P	100 MW
Nominal dc voltage	$V_{\rm dc}$	132 kV
AC grid voltage	$V_{\rm ac}$	66 kV
AC grid frequency	$f_{\rm ac}$	50 Hz
Chopper-cell number per leg	N	64
Chopper-cell capacitance	C	2.5 mF (H_C = 40.8 ms)
Capacitor nominal voltage	V_C	4.125 kV
AC-link inductance	$L_{\rm ac}$	13.9 mH (10%)
Center-tapped inductance	L_Z	27.9 mH (20%)
PWM carrier frequency	$f_{\rm cr}$	75 Hz
Dead time		8 μs

Values in ( ) are on a three-phase, 66 kV, 100 MW, 50 Hz base.

each chopper cell and the response of the controller [38]. Fig. 10 shows that the rotating-carrier PWM can cancel out the dc-voltage component deviation in the arm-side voltage of a chopper cell without compromising the fundamental-frequency component and the controller response.

IV. SIMULATION

A. Three-Phase DSCC Converter With 64 Chopper Cells Per Leg

Fig. 11 shows the circuit diagram of a three-phase grid-connected DSCC converter that is used in this simulation. Table II summarizes the parameters, in which the rated power of the converter is set to 100 MW, and a 132-kV dc voltage source is connected to the dc side of the converter. Each of the ac terminals of the converter is connected to a three-phase 66-kV, 50-Hz utility grid through an ac-link inductor $L_{\rm ac}$. The nominal capacitor voltage in each cell is set to 4.125 kV. The DSCC converter uses 64 triangular carrier signals that are phase-shifted to each other by 5.625° ($= 360^\circ/64$). The PSRC-PWM method is applied with the rotation angle of $\delta = 11.25^\circ$ ($= 360^\circ/32$). Note that the control method for the DSCC converter based on the PSRC-PWM is entirely the same as the one used for the DSCC converter based on PSC-PWM.

For a low number of the chopper cells per leg (for example, $N = 16$), multiple switching instances may occur at the same time because of a relatively large rotating angle δ. In this condition, the PSRC-PWM may produce unwanted voltage spikes at the ac terminals of the DSCC converter when a dead time is introduced to the controller. However, this bad condition can be avoided as the number of chopper cells per leg becomes larger. Further investigation of the PSRC-PWM into a low number of chopper cells is beyond the scope of this paper and left for future work.

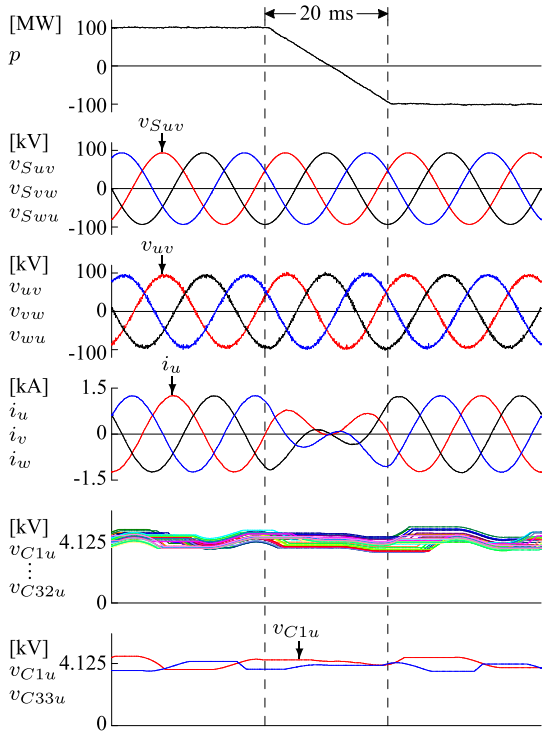

Fig. 12. Simulated waveforms of the 66-kV, 50-Hz, 64-cell grid-connected DSCC converter using the PSRC-PWM with a carrier frequency of 75 Hz (CFR = 3/2) under the rated-power reversal from rectification to inversion during an interval of 20 ms.

This paper provides simulated results that are obtained by using PSCAD/EMTDC software package. The authors of this paper have provided direct comparisons between the experimental waveforms and the simulated ones under the same circuit parameters, control gains, sampling frequency, dead time, and controller delay time [17], [18], [33]. The resulting waveforms are very similar to each other, thus resulting in proving that the simulated waveforms are as reliable as the experimental ones. Hence, although no experimental result is presented here, the authors of this paper believe that the simulation system and its resultant waveforms provided in this paper are adequately reliable.

B. Simulated Results

Fig. 12 shows the voltage and current waveforms of the DSCC converter based on the PSRC-PWM when the power reference p^* is changed from 100 to -100 MW within 20 ms. It can be seen that although the carrier frequency $f_{\rm cr}$ is 75 Hz, the system response to the power reference is still fast while maintaining the balance of the capacitor voltages with the average peak-to-peak voltage fluctuation of 24.1%. The THD value of the line-to-line voltage is 2.56%, whereas the THD value of the line current is as low as 0.92%. The capacitor voltages numbered 1 to 32 in the upper arm of the u-phase are shown because the capacitor voltages numbered 34 to 64 in the lower arm of the u-phase

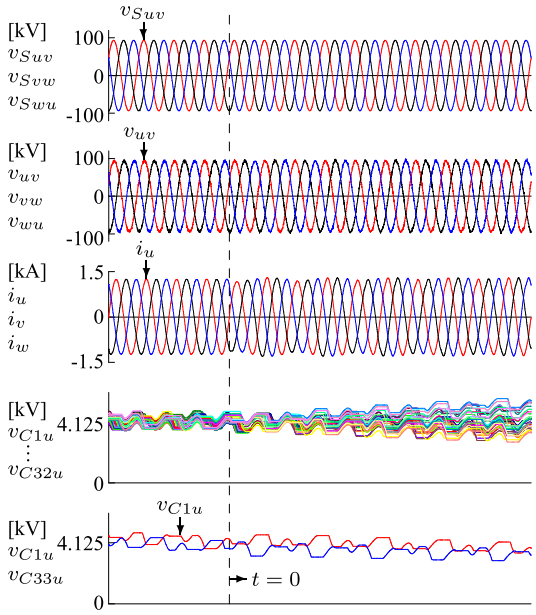

Fig. 13. Simulated waveforms of the 66-kV, 50-Hz, 64-cell grid-connected DSCC converter with a carrier frequency of 75 Hz (CFR $= 3/2$) under the rated rectification and a changeover from the PSRC-PWM to the PSC-PWM at $t = 0$.

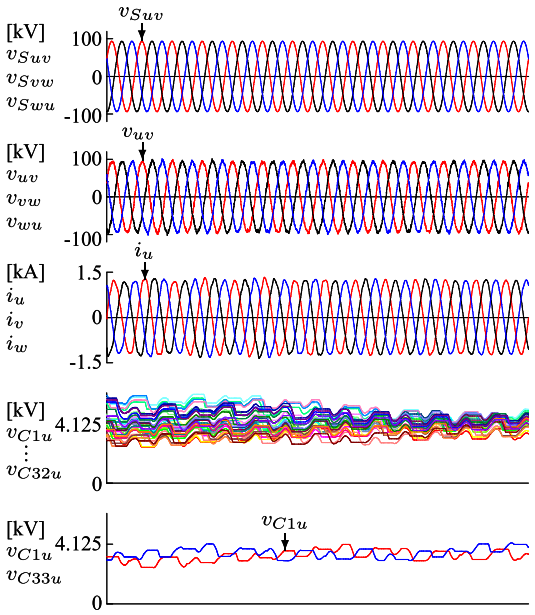

Fig. 14. Simulated waveforms of the 66-kV, 50-Hz, 64-cell grid-connected DSCC converter with a carrier frequency of 75 Hz (CFR $= 3/2$) under the rated rectification when the modulation method is changed back to the PSRC-PWM shortly after it is switched to the PSC-PWM.

(v_{C34u}–v_{C64u}) have similar waveform to the capacitor voltage numbered 33, v_{C33u}, shown at the bottom of Fig. 12.

Fig. 13 shows the voltage and current waveforms of the DSCC converter operating at the rated power with rectification when the PSRC-PWM is changed to the PSC-PWM at $t = 0$. The capacitor voltages start to diverge after the changeover, making the system unstable as the time goes on. This result demonstrates that the PSRC-PWM can reduce significantly dc-component deviations in the capacitor voltages. Note that the control gain of the individual balancing control for eliminating the dc-component deviation can be set to a very low value when the PSRC-PWM is used. However, removing the individual balancing control is not recommended practically to ensure the stability of the capacitor voltages at all time.

Fig. 14 shows the voltage and current waveforms of the DSCC converter operating at the rated power with rectification when the modulation method is changed back to the PSRC-PWM shortly after it is switched to the PSC-PWM, as shown in Fig. 13. Fig. 14 concludes clearly that the PSRC-PWM makes the capacitor voltages converge as the time goes on, and reduces dc-component deviations in the capacitor voltages caused by the PSC-PWM operation. Note that the waveforms in Fig. 14 are obtained by changing only the modulation method, and no change occurs in either capacitor balancing controller or its gain. Although only the 75 Hz carrier frequency is presented in this section, similar results can be shown for other carrier frequencies.

C. Avoidance of Multi-Switchings

A uniform multisampled PWM method offers a better option than the symmetrically or the asymmetrically sampled PWM method that has only one or two samples per carrier period [39], [40]. The uniform multisampled PWM method has not only

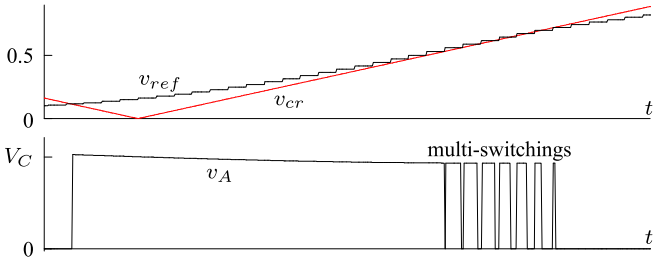

Fig. 15. Occurrence of multiswitchings at the arm-side voltage of a chopper cell, v_A, when a uniform multisampled PWM is used at CFR $= 3/2$.

better fundamental-frequency voltage but also faster PWM controller response time. However, multiswitchings may occur in a multisampled PWM when a relatively low carrier frequency is utilized, even though the CFR is higher than the multiswitching boundary defined by (5).

Fig. 15 shows the occurrence of multiswitchings in a chopper cell as a result of multisampling process of the reference signal v_{ref} that has a sampling period of $1/Nf_{\mathrm{cr}}$. For instance, in a 64-cell DSCC converter utilizing a carrier frequency of 75 Hz, the reference signal v_{ref} in each chopper cell is updated every 208.3 μs.

To avoid multiswitchings, this paper proposes an anti-multiswitch algorithm based on predictive signal sampling of the reference and carrier. The predicted reference-signal value of the next sampling period can be written as

$$v_{\mathrm{ref}}^{+1} = v_{\mathrm{ref}} + K\left(v_{\mathrm{ref}} - v_{\mathrm{ref}}^{-1}\right) \tag{17}$$

where K is a constant gain that defines predicted increment of the reference signal for the next sampling period based on the previous signal sample v_{ref}^{-1}. In a triangular carrier signal, the next sample value can be predicted, based on the sampling

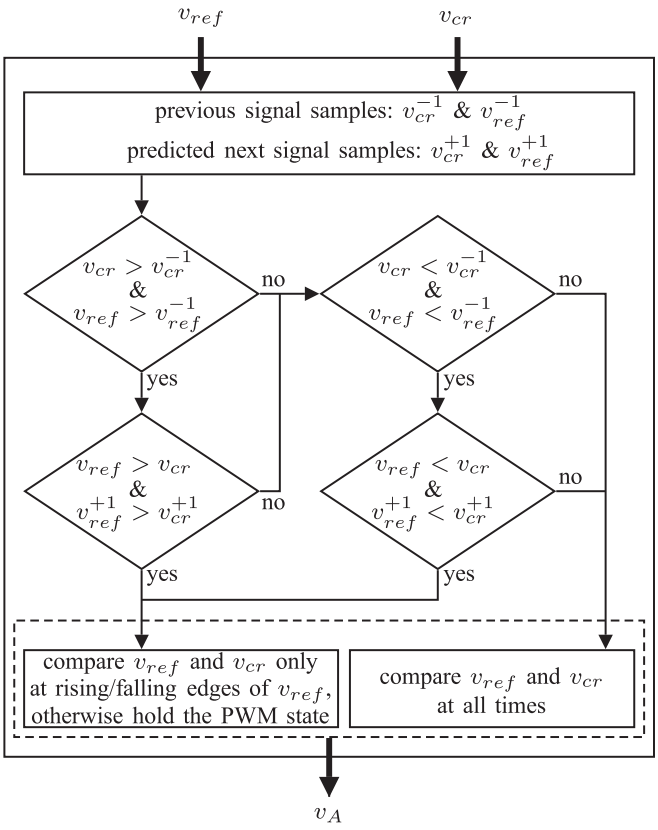

Fig. 16. Additional anti-multiswitch algorithm to avoid multiswitchings caused by the uniform multisampled PWM method.

period or the number of chopper cells per leg. By assuming that the carrier signal has unity amplitude, the predicted carrier signal for the next sampling period can be written as follows:

$$v_{\text{cr}}^{+1} = v_{\text{cr}} + \frac{2}{N}. \tag{18}$$

Fig. 16 shows the proposed anti-multiswitch algorithm. It alters the PWM controller only if the reference and carrier signals are incrementing or decrementing at the same time. For example, assume that both reference and carrier signals are incrementing, and that the reference signal v_{ref} is higher than the carrier signal v_{cr}. If the predicted reference signal v_{ref}^{+1} is still higher than the predicted carrier signal v_{cr}^{+1} at the next sampling period, then the PWM controller compares the two signals only when the reference signal is updated to a new value. As a result, the use of this algorithm can avoid the occurrence of multiswitchings.

Fig. 17 shows a comparison in voltage and current waveforms between the DSCC converter without the anti-multiswitch algorithm and that with it. The predicted reference signal v_{ref}^{+1} is obtained by using a constant gain of $K = 0.9$. Note that the two figures show only the first arm-side voltage of the chopper cells in the u-phase leg, v_{A1u}, the amplitude of which corresponds to the capacitor voltage v_{C1u} at the bottom of the figures. Fig. 17(b) shows that the proposed algorithm produces a very similar arm-side voltage of a chopper cell without causing multiswitchings.

TABLE III
COMPARISONS AMONG SEVERAL CARRIER-FREQUENCY RATIOS IN A RANGE OF $1 < \text{CFR} \leq 2$ USED IN THE DSCC CONVERTER

f_{cr} [Hz]	CFR	f_L [Hz]	f_{sw} [Hz]	ΔV_{Adc}	THD_i [%]	$\overline{V}_{\text{Cpp}}$ [%]
60	6/5	10	66.3[1]	+[2]	1.19	34
62.5	5/4	12.5	70.7[1]	0	1.68	31.8
66.7	4/3	16.7	73[1]	++[2]	1.25	27.7
70	7/5	10	72.5[1]	0	0.97	27.5
75	3/2	25	77.3	0	0.92	24.1
80	8/5	10	82.5	+[2]	2.12	22.7
83.3	5/3	16.7	85.9	0	1.22	22.5
87.5	7/4	12.5	90.2	0	0.95	22.4
90	9/5	10	92.8	0	0.71	24.8
100	2/1	50	103.1	0	1.54	24.4

[1] maximum switching frequency. [2] deviation: (++) large; (+) small.

V. OPTIMAL LOW-CARRIER-FREQUENCY RATIO WITH PSRC-PWM

The PSRC-PWM method can eliminate CFR limitation from the DSCC converter as discussed in Section III. It is concluded in [32], [33] that the CFRs of $2/1$ and $3/1$ result in unstable operation when the PSC-PWM is used. However, it can be shown that the two CFRs yield stable operation when the PSRC-PWM is utilized. This section dedicates itself to the optimal CFR when the carrier frequency f_{cr} is lower than double the ac grid frequency ($2f_{\text{ac}}$).

This paper defines five performance criteria to compare several carrier frequencies as follows:

1) the lowest harmonic frequency of capacitor voltage f_L [33];
2) equivalent switching frequency f_{sw};
3) dc-component deviation in the arm-side voltage of a chopper cell, ΔV_{Adc};
4) line current THD;
5) peak-to-peak capacitor voltage fluctuation V_{Cpp}.

Table III summarizes the performance comparison among several carrier frequencies for the three-phase PSRC-PWM-based DSCC converter with 64 chopper cells per leg along with the parameters listed in Table II. The results in Table III are obtained by using analytical and numerical analyses, as well as the circuit simulation described in Section IV-A. The carrier frequencies are selected in such a way that each CFR is a rational number with an integer number of f'_{ac}. In this way, the lowest harmonic frequency of each capacitor voltage f_L is not too close to zero. There are some CFRs where the dc-component deviation ΔV_{Adc} cannot be eliminated even if the PSRC-PWM is used. Thus, they should be avoided to guarantee proper operation. Note that the equivalent switching frequency f_{sw} is not always the same as (9) when the CFR is lower than the ratio limit CFR_B at high modulation indices M.

The CFR of 2/1 results in stable operation, and has the highest frequency in f_L. However, the line current THD and the peak-to-peak capacitor–voltage fluctuation V_{Cpp} are relatively higher than the other CFRs that are lower than 2/1. Among the carrier frequencies, the CFR of $3/2$ can be considered as the optimal ratio because it results in low and constant switching

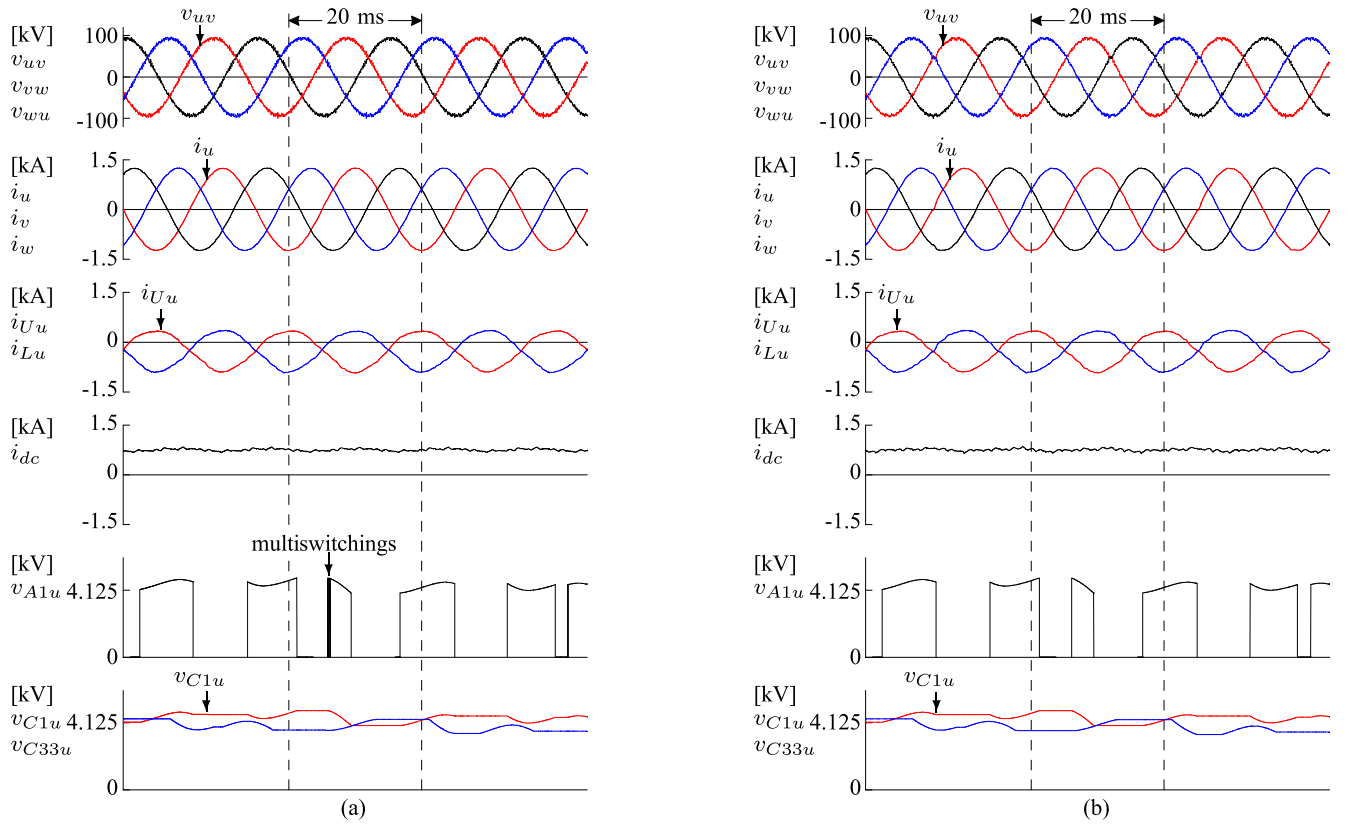

Fig. 17. Simulated waveforms of the 66-kV, 50-Hz, PSRC-PWM-based DSCC converter having 64 chopper cells per leg with a carrier frequency of 75 Hz (CFR $= 3/2$) at the rated power in rectification mode: (a) without anti-multiswitch algorithm; (b) and with anti-multiswitch algorithm.

frequency f_{sw}, produces no dc deviation in the arm-side voltage of a chopper cell ($\Delta V_{\text{Adc}} = 0$), and has a relatively low average peak-to-peak capacitor–voltage fluctuation $\overline{V}_{\text{Cpp}}$. Moreover, the lowest frequency component f_L is the second highest frequency among the CFRs, which means that the moving-average filter has the second fastest response. The other CFRs are also applicable as long as no dc-component deviation occurs. However, the response of the moving-average filter might be slower.

VI. Conclusion

This paper has proposed a PSRC-PWM method for a DSCC converter intended for high-power applications. The PSRC-PWM method opens the possibility of using a low switching frequency, providing the capability of balancing the capacitor voltages of all chopper cells. Moreover, the PSRC-PWM method with low carrier frequencies can eliminate dc-voltage deviation from the chopper cells. Analytical approach based on double-variable Fourier series has been adopted to derive harmonic-voltage equations at the arm-side of a chopper cell. Circuit simulation has been carried out to confirm the validity of theoretical and numerical analyses. Simulated waveforms obtained from a three-phase 66-kV, 50-Hz, 100-MW, 132-kVdc grid-connected DSCC converter with 64 chopper cells per leg have shown that the PSRC-PWM method makes the DSCC converter stable, and maintain the capacitor voltages balanced. Based on several performance criteria, it has been concluded that the optimal carrier frequency is 75 Hz in a range of 50–100 Hz.

Appendix
Geometrical Representation of Rotating-Carrier PWM Based on Double-Variable Fourier Series

Fig. 18 shows a two-dimensional model of double-edge naturally sampled PWM, leading to providing a geometric representation of the modulation processes when a nonrotating carrier and a rotating carrier is used. The representation of a PWM waveform by a wall function $F(x, y)$ can specify the exact harmonic spectrum analytically by using double-variable Fourier series. The x and y variables in the function $F(x, y)$ can be regarded as the time function of the carrier signal $x(t) = \omega_{\text{cr}}t + \theta_{\text{cr}}$ and the reference signal $y(t) = \omega_{\text{ac}}t + \theta_{\text{ac}}$, respectively. In a two-level PWM process, such as in the arm-side voltage of a chopper cell, the height of the function $F(x, y)$ takes either 0 or 1, as shown in Fig. 18.

The slope of the frequency ratio $(1/\text{CFR})$ of the rotating carrier becomes a flat line every carrier cycle due to the rotation angle δ. The flat lines and the striped areas along the y-axis represent a phase jump in the carrier signal. These areas are not accounted for the mathematical integration in the double Fourier series but they show clearly the equivalent angular cycle of the rotating carrier τ_R. Fig. 18 shows that the angular cycle of the wall function using a rotating carrier in the x-axis, with respect

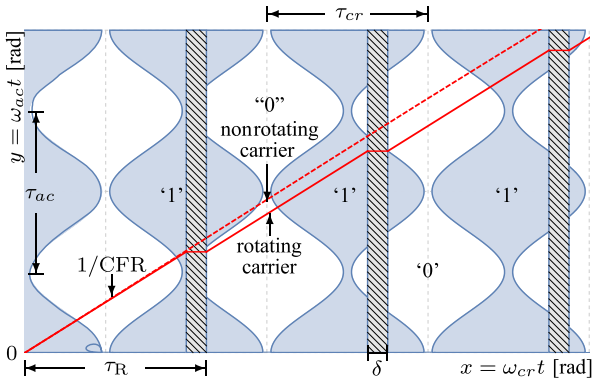

Fig. 18. Two-dimensional geometrical representation of a two-level naturally sampled PWM using a nonrotating carrier and a rotating carrier.

to the carrier angular cycle $\tau_{\rm cr} = 2\pi$, is given as follows:

$$\tau_R = 2\pi + \delta. \tag{19}$$

A periodic carrier signal waveform is required to obtain the harmonic-voltage spectrum at the arm side of a chopper cell when the rotating-carrier PWM is applied. For example, nine carrier cycles are required for a periodic rotating-carrier signal with $\delta = \pi/4$ as shown in Fig. 6. If the amplitude of each harmonic spectrum in the Fourier series can be represented by a complex number $C_{\rm mn}$, where m is the carrier index variable and n is the reference or baseband index variable, then the double-edge naturally sampled PWM function using a rotating carrier for $N/2$ carrier cycles can be derived as follows:

$$\begin{aligned} F_R(x,y) = {} & \frac{1}{2} + \frac{1}{2}M\cos(\omega_{\rm ac}t + \theta_{\rm ac}) \\ & + \sum_{\rm m=1}^{\infty} |C_{\rm m0}| \cos\left(m'\omega_{\rm cr}t + \theta_{\rm m0}\right) \\ & + \sum_{\rm m=1}^{\infty}\sum_{\substack{n=-\infty \\ n\neq 0}}^{\infty} |C_{\rm mn}| \\ & \times \cos\left(m'\omega_{\rm cr}t + n\omega_{\rm ac}t + \theta_{\rm mn}\right) \end{aligned} \tag{20}$$

where $m' = 2m/N$. The complex numbers $C_{\rm m0}$ and $C_{\rm mn}$, and the phase components $\theta_{\rm m0}$ and $\theta_{\rm mn}$ are defined as follows:

$$\begin{aligned} C_{\rm m0} = {} & \frac{2}{m\pi}\sum_{\rm l=1}^{N/2}\left\{\frac{\psi_l}{\pi}\sin(m'\pi)\left\{e^{{\rm j}m'\lambda_l} - J_0\left(m'\frac{\pi}{2}M\right)\right.\right. \\ & \left.\times e^{{\rm j}m'(\lambda_l+\delta_l)}e^{\mp{\rm j}m'\frac{\pi}{2}}\right\} \\ & + J_0\left(m'\frac{\pi}{2}M\right)\sin\left(m'\frac{\pi}{2}\right)e^{{\rm j}m'(\lambda_l+\delta_l)} \\ & - 2\sin(m'\pi)e^{{\rm j}m'(\lambda_l+\delta_l)}\sum_{\rm k=1}^{\infty}\frac{1}{\pi k}\sin(k\psi_l) \\ & \left.\times J_k\left(m'\frac{\pi}{2}M\right)e^{\mp j\frac{\pi}{2}(m'-k)}\right\} \end{aligned} \tag{21}$$

$$\begin{aligned} C_{\rm mn} = {} & \frac{2}{m\pi}\sum_{\rm l=1}^{N/2}\left\{\frac{1}{n\pi}\sin(m'\pi)\sin(n\psi_l)\left\{e^{{\rm j}m'\lambda_l}\right.\right. \\ & \left. - J_0\left(m'\frac{\pi}{2}M\right)e^{{\rm j}m'(\lambda_l+\delta_l)}e^{\mp{\rm j}m'\frac{\pi}{2}}\right\} \\ & - \frac{1}{2\pi}J_n\left(m'\frac{\pi}{2}M\right)\left(\frac{\sin(2n\psi_l)}{2} + 2\psi_l\right) \\ & \times \sin\left(m'\pi\right)e^{{\rm j}m'(\lambda_l+\delta_l)}e^{\mp j\frac{\pi}{2}(m'-n)} \\ & + J_n\left(m'\frac{\pi}{2}M\right)\sin\left((n+m')\frac{\pi}{2}\right)e^{{\rm j}m'(\lambda_l+\delta_l)} \\ & - \sin(m'\pi)e^{{\rm j}m'(\lambda_l+\delta_l)}\sum_{\substack{k=1 \\ k\neq|n|}}^{\infty}J_k\left(m'\frac{\pi}{2}M\right) \\ & \times\left\{\frac{\sin(\psi_l({\rm n}+{\rm k}))}{\pi(n+k)} + \frac{\sin(\psi_l({\rm n}-{\rm k}))}{\pi(n-k)}\right\} \\ & \left.\times e^{\mp j\frac{\pi}{2}(m'-k)}\right\} \end{aligned} \tag{22}$$

$$\theta_{\rm m0} = \theta_{\rm cr} - \tan^{-1}\frac{{\rm Im}(C_{\rm m0})}{{\rm Re}(C_{\rm m0})}, \tag{23}$$

$$\theta_{\rm mn} = (m'\theta_{\rm cr} + n\theta_{\rm ac}) - \tan^{-1}\frac{{\rm Im}(C_{\rm mn})}{{\rm Re}(C_{\rm mn})} \tag{24}$$

where l and k are positive integers, $J_y(x)$ is the y-order Bessel function of the first kind, and λ_l and δ_l are the angle variables for each unique wall within a rotating-carrier angular cycle τ_R, and are given as follows:

$$\lambda_l = \frac{2\pi}{N}(2l-1), \tag{25}$$

$$\delta_l = \pi - \delta(l-1). \tag{26}$$

The length ψ_l in the y-axis direction and the minus-plus sign ($\mp$) appearing in (21) and (22) can be related to the angle δ_l in the range of $-\pi \le \delta_l \le \pi$ as follows:

$$\psi_l = \cos^{-1}\left(\frac{\pi - 2|\delta_l|}{M\pi}\right) \tag{27}$$

$$\mp = \begin{cases} -, & \text{for } 0 \le \delta_l \le \pi \\ +, & \text{for } -\pi \le \delta_l \le 0. \end{cases} \tag{28}$$

REFERENCES

[1] N. Flourentzou, V. G. Agelidis, and G. D. Demetriades, "VSC-based HVDC power transmission systems: An overview," *IEEE Trans. Power Electron.*, vol. 24, no. 30, pp. 592–602, Mar. 2009.

[2] A. M. Abbas and P. W. Lehn, "PWM based VSC-HVDC systems—A review," in *Proc. IEEE Power Energy Soc. Gen. Meet.*, 2009, pp. 1–9.

[3] J. Glasdam, J. Hjerrild, L. H. Kocewiak, and C. L. Bak, "Review on multi-level voltage source converter based HVDC technologies for grid connection of large offshore wind farms," in *Proc. IEEE Int. Conf. Power Syst. Technol.*, 2012, pp. 1–6.

[4] S. Kouro "Recent advances and industrial applications of multilevel converters," *IEEE Trans. Power Electron.*, vol. 57, no. 8, pp. 2553–2580, Aug. 2010.

[5] M. A. Perez, S. Bernet, J. Rodriguez, S. Kouro, and R. Lizana, "Circuit topologies, modeling, control schemes, and applications of modular multilevel converters," *IEEE Trans. Power Electron.*, vol. 30, no. 1, pp. 4–17, Jan. 2015.
[6] S. Debnath, J. Qin, B. Bahrani, M. Saeedifard, and P. Barbosa, "Operation, control, and applications of the modular multilevel converter: A review," *IEEE Trans. Power Electron.*, vol. 30, no. 1, pp. 37–53, Jan. 2015.
[7] R. Marquardt and A. Lesnicar, "A new modular voltage source inverter topology," in *Proc. Eur. Power Electron. Conf.*, 2003, pp. 2–4.
[8] M. Glinka and R. Marquardt, "A new ac/ac multilevel converter family," *IEEE Trans. Ind. Electron.*, vol. 52, no. 3, pp. 662–669, Jun. 2005.
[9] S. Allebrod, R. Hamerski, and R. Marquardt, "New transformerless, scalable modular multilevel converters for HVDC-transmission," in *Proc. IEEE Power Electron. Spec. Conf.*, 2008, pp. 174–179.
[10] H. Akagi, "Classification, terminology, and application of the modular multilevel cascade converter (MMCC)," *IEEE Trans. Power Electron.*, vol. 26, no. 11, pp. 3119–3130, Nov. 2011.
[11] X. Shi, Z. Wang, L. M. Tolbert, and F. Wang, "A comparison of phase disposition and phase shift PWM strategies for modular multilevel converters," in *Proc. IEEE Energy Convers. Congr. Expo.*, 2013, pp. 4089–4096.
[12] A. Hassanpoor, S. Norrga, H.-P. Nee, and L. Angquist, "Evaluation of different carrier-based PWM methods for modular multilevel converters for HVDC application," in *Proc. 38th Annu. Conf. IEEE Ind. Electron. Soc.*, 2012, pp. 388–393.
[13] M. Saeedifard and R. Iravani, "Dynamic performance of a modular multilevel back-to-back HVDC system," *IEEE Trans. Power Del.*, vol. 25, no. 4, pp. 2903–2912, Oct. 2010.
[14] J. Mei, B. Xiao, K. Shen, L. M. Tolbert, and J. Y. Zhen, "Modular multilevel inverter with new modulation method and its application to photovoltaic grid-connected generator," *IEEE Trans. Power Electron.*, vol. 28, no. 11, pp. 5063–5073, Nov. 2013.
[15] S. Fan, K. Zhang, J. Xiong, and Y. Xue, "An improved control system for modular multilevel converters with new modulation strategy and voltage balancing control," *IEEE Trans. Power Electron.*, vol. 30, no. 1, pp. 358–371, Jan. 2015.
[16] M. Hagiwara and H. Akagi, "Control and experiment of pulsewidth-modulated modular multilevel converters," *IEEE Trans. Power Electron.*, vol. 24, no. 7, pp. 1737–1746, Jul. 2009.
[17] K. Sekiguchi, P. Khamphakdi, M. Hagiwara, and H. Akagi, "A grid-level high-power BTB (back-to-back) system using modular multilevel cascade converters without common dc-link capacitor," *IEEE Trans. Ind. Appl.*, vol. 50, no. 4, pp. 2648–2659, Jul./Aug. 2014.
[18] P. Khamphakdi, K. Sekiguchi, M. Hagiwara, and H. Akagi, "A transfomerless back-to-back (BTB) system using modular multilevel cascade converters for power distribution systems," *IEEE Trans. Power Electron.*, vol. 30, no. 4, pp. 1866–1875, Apr. 2015.
[19] B. Li, R. Yang, D. Xu, G. Wang, W. Wang, and D. Xu, "Analysis of the phase-shifted carrier modulation for modular multilevel converters," *IEEE Trans. Power Electron.*, vol. 30, no. 1, pp. 297–310, Jan. 2015.
[20] R. Darus, J. Pou, G. Konstantinou, S. Ceballos, R. Picas, and V. G. Agelidis, "A modified voltage balancing algorithm for the modular multilevel converter: Evaluation for staircase and phase-disposition PWM," *IEEE Trans. Power Electron.*, vol. 30, no. 8, pp. 4119–4127, Aug. 2015.
[21] M. S. A. Dahidah, G. Konstantinou, and V. G. Agelidis, "A review of multilevel selective harmonic elimination PWM: Formulations, solving algorithms, implementation and applications," *IEEE Trans. Power Electron.*, vol. 30, no. 8, pp. 4091–4106, Aug. 2015.
[22] Q. Tu and Z. Xu, "Impact of sampling frequency on harmonic distortion for modular multilevel converter," *IEEE Trans. Power Del.*, vol. 26, no. 1, pp. 298–306, Jan. 2011.
[23] S. Rohner, S. Bernet, M. Hiller, and R. Sommer, "Modulation, losses, and semiconductor requirements of modular multilevel converters," *IEEE Trans. Ind. Electron.*, vol. 57, no. 8, pp. 2633–2642, Aug. 2010.
[24] Z. Li, P. Wang, H. Zhu, Z. Chu, and Y. Li, "An improved pulse width modulation method for chopper-cell-based modular multilevel converters," *IEEE Trans. Power Electron.*, vol. 27, no. 8, pp. 3472–3481, Aug. 2012.
[25] P. Hu and D. Jiang, "A level-increased nearest level modulation method for modular multilevel converters," *IEEE Trans. Power Electron.*, vol. 30, no. 4, pp. 1836–1842, Apr. 2015.
[26] S. Du, J. Liu, and T. Liu, "Modulation and closed-loop-based dc capacitor voltage control for MMC with fundamental switching frequency," *IEEE Trans. Power Electron.*, vol. 30, no. 1, pp. 327–338, Jan. 2015.
[27] P. M. Meshram and V. B. Bhorgate, "A simplified nearest level control (NLC) voltage balancing method for modular multilevel converter (MMC)," *IEEE Trans. Power Electron.*, vol. 30, no. 1, pp. 450–462, Jan. 2015.
[28] K. Ilves, L. Harnerfors, S. Norrga, and H-. P. Nee, "Predictive sorting algorithm for modular multilevel converters minimizing the spread in the submodule capacitor voltages," *IEEE Trans. Power Electron.*, vol. 30, no. 1, pp. 440–449, Jan. 2015.
[29] K. Ilves, A. Antonopoulos, S. Norrga, and H. P. Nee, "A new modulation method for the modular multilevel converter allowing fundamental switching frequency," *IEEE Trans. Power Electron.*, vol. 27, no. 8, pp. 3482–3494, Aug. 2012.
[30] A. Hassanpoor, L. Angquist, S. Norrga, K. Ilves, and H.-P. Nee, "Tolerance band modulation methods for modular multilevel converters," *IEEE Trans. Power Electron.*, vol. 30, no. 1, pp. 311–326, Jan. 2015.
[31] Q. Tu, Z. Xu, and L. Xu, "Reduced switching-frequency modulation and circulating current suppression for modular multilevel converters," *IEEE Trans. Power Del.*, vol. 26, no. 3, pp. 2009–2017, Jul. 2011.
[32] K. Ilves, L. Harnefors, S. Norrga, and H.-P. Nee, "Analysis and operation of modular multilevel converters with phase-shifted carrier PWM," *IEEE Trans. Power Electron.*, vol. 30, no. 1, pp. 268–283, Jan. 2015.
[33] F. Sasongko, K. Sekiguchi, K. Oguma, M. Hagiwara, and H. Akagi, "Theory and experiment on an optimal carrier frequency of a modular multilevel cascade converter with phase-shifted PWM," *IEEE Trans. Power Electron.*, vol. 31, no. 5, pp. 3456–3471, May 2016.
[34] H. Fujita, S. Tominaga, and H. Akagi, "Analysis and design of a dc voltage-controlled static var compensator using quad-series voltage-source inverters," *IEEE Trans. Ind. Appl.*, vol. 32, no. 4, pp. 970–978, Jul./Aug. 1996.
[35] D. G. Holmes and T. A. Lipo, *Pulse Width Modulation for Power Converters: Principles and Practice*. New York, NY, USA: Wiley-IEEE Press, 2003.
[36] H. S. Black, *Modulation Theory*. New York, NY, USA: D. Van Nostrad Company, 1953.
[37] S. R. Bowes and B. M. Bird, "Novel approach to the analysis and synthesis of modulation processes in power converters," *Proc. Inst. Electr. Eng.*, vol. 122, no. 5, pp. 507–513, 1975.
[38] G. Walker and G. Ledwich, "Bandwidth considerations for multilevel converters," *IEEE Trans. Power Electron.*, vol. 14, no. 1, pp. 74–81, Jan. 1999.
[39] G. R. Walker, "Digitally-implemented naturally sampled PWM suitable for multilevel converter control," *IEEE Trans. Power Electron.*, vol. 18, no. 6, pp. 1322–1329, Nov. 2003.
[40] X. Zhang and J. W. Spencer, "Study of multisampled multilevel inverters to improve control performance," *IEEE Trans. Power Electron.*, vol. 27, no. 11, pp. 4409–4416, Nov. 2012.

Firman Sasongko (S'13) was born in Jakarta, Indonesia, in 1985. He received the B.S. and M.S. degrees in electrical engineering from the Bandung Institute of Technology, Bandung, Indonesia, in 2008 and 2011, respectively, and the Ph.D. degree in electrical engineering from the Tokyo Institute of Technology, Tokyo, Japan, in 2016.

His research interests include high-voltage and high-power converters and their applications.

Hirofumi Akagi (M'87–SM'94–F'96) was born in Okayama, Japan, in 1951. He received the Ph.D. degree in electrical engineering from the Tokyo Institute of Technology, Tokyo, Japan, in 1979.

Since 2000, he has been a Professor in the Department of Electrical and Electronic Engineering, Tokyo Institute of Technology. Prior to it, he was with the Nagaoka University of Technology, Nagaoka, Japan, and Okayama University, Okayama, Japan. His research interests include power conversion systems and its applications to industry, transportation, and utility. He has authored and coauthored some 120 IEEE Transactions papers.

Dr. Akagi received six IEEE Transactions Prize Paper Awards and 15 IEEE Industry Applications Society (IAS) Committee Prize Paper Awards, the 2001 IEEE William E. Newell Power Electronics Award, the 2004 IEEE IAS Outstanding Achievement Award, the 2008 IEEE Richard H. Kaufmann Technical Field Award, the 2012 IEEE PES Nari Hingorani Custom Power Award, and the 2014 EPE Outstanding Service Award. He served as the President of the IEEE Power Electronics Society during 2007–2008. Since 2015, he has been serving as the IEEE Division II Director.